RSC Advances

PAPER

View Article Online
View Journal | View Issue

Cite this: *RSC Adv.*, 2023, **13**, 12344

Self-supporting network-structured MoS_2/heteroatom-doped graphene as superior anode materials for sodium storage†

Guanhua Yang,[ab] Xu Wang,[a] Yihong Li,[a] Zhiguo Zhang,[a] Jiayu Huang,[a] Fenghua Zheng,[b] Qichang Pan,[b] Hongqiang Wang,*[b] Qingyu Li[b] and Yezheng Cai*[b]

Layered graphene and molybdenum disulfide have outstanding sodium ion storage properties that make them suitable for sodium-ion batteries (SIBs). However, the easy and large-scale preparation of graphene and molybdenum disulfide composites with structural stability and excellent performance face enormous challenges. In this study, a self-supporting network-structured MoS_2/heteroatom-doped graphene (MoS_2/NSGs-G) composite is prepared by a simple and exercisable electrochemical exfoliation followed by a hydrothermal route. In the composite, layered MoS_2 nanosheets and heteroatom-doped graphene nanosheets are intertwined with each other into self-supporting network architecture, which could hold back the aggregation of MoS_2 and graphene effectively. Moreover, the composite possesses enlarged interlayer spacing of graphene and MoS_2, which could contribute to an increase in the reaction sites and ion transport of the composite. Owing to these advantageous structural characteristics and the heteroatomic co-doping of nitrogen and sulfur, MoS_2/NSGs-G demonstrates greatly reversible sodium storage capacity. The measurements revealed that the reversible cycle capacity was 443.9 mA h g^{-1} after 250 cycles at 0.5 A g^{-1}, and the rate capacity was 491.5, 490.5, 453.9, 418.1, 383.8, 333.1, and 294.4 mA h g^{-1} at 0.1, 0.2, 0.5, 1, 2, 5 and 10 A g^{-1}, respectively. Furthermore, the MoS_2/NSGs-G sample displayed lower resistance, dominant pseudocapacitive contribution, and faster sodium ion interface kinetics characteristic. Therefore, this study provides an operable strategy to obtain high-performance anode materials, and MoS_2/NSGs-G with favorable structure and excellent cycle stability has great application potential for SIBs.

Received 24th December 2022
Accepted 29th March 2023

DOI: 10.1039/d2ra08207a

rsc.li/rsc-advances

1. Introduction

In the past few years, lithium-ion batteries (LIBs) have been used in portable electronic devices and electric vehicles on a large scale because of the advantages of high capacity, high working voltage, long cycle life, and high safety.[1–4] With the development of society, the huge demands for LIBs have become even stronger. However, the low abundance of lithium content in the Earth's crust and the rising lithium prices would seriously restrict the LIB's further application.[5,6] Therefore, the exploration of other new and inexpensive alternative or complementary LIBs energy storage technology is particularly critical.[7,8] SIB is considered a new type of secondary battery with great development prospects due to the advantages of abundant sodium resources, good safety, and low cost, which is of great strategic significance for the sustainable development of energy globally.[9,10]

Although SIBs have a similar energy storage mechanism to LIBs, it is difficult to directly use the commercial graphite anode in SIBs. This is due to the mismatch between the graphite-layer spacing and the sodium-ion size, the spacing of graphite layers is only 39% larger than the diameter of the sodium ion (0.335 nm for the spacing of graphite layers *vs.* 0.204 nm for the diameter of the sodium ion), which leads to low reversible capacity, sluggish electrochemical reaction kinetics and poor cycling stability.[11–14] In addition, although the capacity of hard carbon materials is 200–400 mA h g^{-1}, its capacity is still low.[15] The uneven and continuous growth of the SEI layer in the charging and discharging process will inhibit the migration of sodium ions and electrons, resulting in problems of low initial coulombic efficiency, largely irreversible capacity loss, low cycle, and rate performance of hard carbon.[16–19] Therefore, it is greatly

[a]*Guangxi Key Laboratory of Automobile Components and Vehicle Technology, School of Mechanical and Automotive Engineering, Guangxi University of Science and Technology, Liuzhou, 545006, China*

[b]*Guangxi Key Laboratory of Low Carbon Energy Materials, Guangxi New Energy Ship Battery Engineering Technology Research Center, Guangxi Scientific and Technological Achievements Transformation Pilot Research Base of Electrochemical Energy Materials and Devices, School of Chemistry and Pharmaceutical Sciences, Guangxi Normal University, Guilin 541004, China. E-mail: yezhengcai@163.com; whq74@gxnu.edu.cn*

† Electronic supplementary information (ESI) available. See DOI: https://doi.org/10.1039/d2ra08207a

essential and urgent to explore proper anode materials with a high specific capacity, long cycle stability, and excellent kinetics to promote the development of SIBs.

In order to obtain excellent performance of anode materials for SIBs, researchers have conducted extensive and in-depth studies on some metal sulfides (MoS_2,[20] SnS_2,[21] Co_9S_8,[22] FeS_2,[23] *etc.*). Among many metal sulfides, MoS_2 has a unique layered structure of a large layer spacing between Mo–S layers (about 0.62 nm), which would facilitate the insertion and removal reaction of sodium and can provide a fast transmission channel for ions.[24] In terms of energy storage, MoS_2 has a high theoretical specific capacity of sodium storage, up to about 670 mA h g^{-1}, which is much higher than the specific capacity of carbonaceous anode materials.[25] Moreover, MoS_2 also has the advantages of abundant raw materials and low cost, showing great commercial application potential in energy storage and energy transformation. However, in practical applications, MoS_2 is prone to structural collapse during the cyclic process due to the semiconductor characteristics of MoS_2 and its huge volume effect, which eventually leads to rapid attenuation of reversible specific capacity and deterioration of cycle performance of the batteries.[26] In addition, the volume effect of MoS_2 would destroy the structure of the electrode material, resulting in an uneven distribution of Na_2S and Mo, and poor diffusion kinetics between Mo and S, which makes the process of regenerating MoS_2 irreversible.[27,28] Therefore, it is necessary to improve the reversibility of the MoS_2 conversion reaction to obtain MoS_2-based anode materials with high capacity and long cycle life for SIBs.

In order to improve the reversibility and conductivity of MoS_2, the researchers have developed MoS_2 and carbon as anode materials for SIB, such as MoS_2/C, MoS_2/graphene, and MoS_2/CNT.[29–31] The carbonaceous material can not only enhance the conductivity of the composite material and slow down the volume effect of MoS_2 but also enhance the mass transfer kinetics of the Na_2S and Mo interface, promoting the transformation reaction of regenerating MoS_2, so as to improve the reversibility of sodium insertion and removal reaction of the composite.[32] Among carbonaceous materials, graphene is favored by researchers for its large surface area, good electrical conductivity, and machinability. Especially, studies have shown that heteroatom (N, S, *etc.*) doped graphene could improve the performance of electrode materials because the introduction of heteroatoms helps to tune the charge state of the material, accelerate the transmission of electrons and increase the active sites of sodium storage.[33–35] However, most reported heteroatom-doped graphene is usually obtained by Hummers', CVD, mechanical stripping or silicon carbide epitaxy, *etc.*[36] These methods involve corrosive reagents, harsh experimental conditions, or complicated impurity removal processes, which would cause environmental pressure and increase the difficulty of operation. In addition, the prepared graphene has a large number of defects and partial oxidation; it is still difficult to be completely reduced even after high-temperature heat treatment, resulting in reduced conductivity and crystallinity of graphene. Therefore, it is necessary to explore an environmentally friendly and easy operation method to prepare heteroatom-doped graphene with good crystallinity to support MoS_2.

Herein, we propose an effective strategy to prepare molybdenum disulfide and heteroatom-doped graphene composites. First, an aqueous solution containing nitrogen and sulfur co-doped graphene was prepared *via* a simple electrochemical exfoliation method without involving strong acids and strong oxidants, which can skillfully avoid excessive oxidation of graphene, permanent defects, and a complex purification process. Then, we directly used a heteroatom-doped graphene aqueous solution to synthesize MoS_2/NSGs-G by the hydrothermal method. In this designed hybrid, nitrogen, and sulfur co-doped graphene can not only enhance the conductivity of the composite but also buffer the volume change of MoS_2 during the sodiation/desodiation process. On the other hand, the few-layered MoS_2 can offer more active sites for sodium ion storage as well as facilitate fast Na^+ insertion/extraction. As a result, when evaluated as an anode material for SIBs, the MoS_2/NSGs-G composite shows superior rate performance and excellent cycling stability.

2. Experimental

2.1 Material reagent

Sodium sulfate (Na_2SO_4, Aladdin), glycine ($C_2H_5NO_2$, Aladdin), dimethyl formamide (DMF, Aladdin), cetrimonium bromide (CTAB, Aladdin), sodium molybdate ($Na_2MoO_4 \cdot 2H_2O$, Aladdin), and L-cysteine ($C_3H_7NO_2S$, Aladdin) were used.

2.2 Preparation of heteroatom-doped graphene

In this preparation process, the nitrogen and sulfur co-doped graphene was obtained by a facile electrochemical exfoliation approach. The electrolyte was composed of sodium sulfate (14.20 g) and glycine (7.51 g) dissolved in 1000 mL of deionized water. Then, the graphite foil (as a working electrode, about 4 cm × 12 cm) and Pt foil (as a counter electrode) were connected to a two-electrode system for electrochemical exfoliation. The height of the graphite foil above the solution level was about 2 cm, and the distance between the two electrodes was maintained around 3 cm throughout the exfoliation process. To improve the hydrophilicity of the graphite foil, the pre-electrochemical exfoliation voltage was set to 2 V and kept for 5 min. Then, a voltage of 10 V was applied between the two electrodes to start the electrochemical exfoliation until the graphite foil was completely exfoliated. Afterward, the black suspension was filtered and repeatedly washed with deionized water and ethanol several times. To obtain fewer-layered graphene, the exfoliated graphene was dispersed into dimethyl formamide and sonicated for 2 h. Then, the dispersion was filtered and washed repeatedly with deionized water to remove dimethyl formamide. After that, the exfoliated graphene was dispersed in deionized water and centrifuged at 3000 rpm for 30 min. Finally, the top part of the suspension was collected and the obtained nitrogen and sulfur co-doped graphene nanosheets were defined as NSGs-G. The nitrogen and sulfur co-

doped graphene nanosheets were confirmed by XPS testing, which displayed that there were bonding states of C–N and C–S in the graphene nanosheets (as shown in Fig. S1†).

2.3 Preparation of MoS_2/heteroatom-co-doped graphene composite

The as-prepared black suspension containing 30 mg NSGs-G was diluted to form an 80 mL aqueous solution and ultrasonic treatment for 1 h. In order to increase the adsorption capacity of graphene onto MoO_4^{2-}, the cetrimonium bromide was added to the above solution and the solution was stirred continuously for 12 h. Then, L-cysteine (1.2 g) and $Na_2MoO_4 \cdot 2H_2O$ (0.6 g) were added to the mixed solution and the solution was stirred for another 2 h. Afterwards, the above solution was transferred to a 100 mL Teflon-lined stainless-steel autoclave to carry out a hydrothermal reaction at the temperature of 200 °C for 24 h. When the autoclave was naturally cooled, the mixture was filtered and washed repeatedly with deionized water and ethanol for several times, then the mixture was dried at 80 °C. To improve the conductivity of the material, the resultant black mixture was heated in the argon atmosphere from room temperature to 800 °C with a heating rate of 3 °C min^{-1} and kept at 800 °C for 2 h. The final product was defined as MoS_2/NSGs-G. In the same way, the MoS_2/Gs composite and bulk MoS_2 were obtained without adding glycine and graphene, respectively.

2.4 Material characterization

The X-ray diffraction (XRD) characterization of the materials was implemented by Rigaku's D/max 2500v/pc instrument using Cu Kα radiation ($\lambda = 0.154$ nm). Field emission scanning electron microscopy (FESEM, Philips' FEI Quanta 200 FEG) and high-resolution transmission electron microscopy (HRTEM, JEOL 2100F) were used to investigate the morphologies of the materials. An energy dispersive spectroscope (EDS, INCA) was connected to the FESEM to analyze the element distribution of the materials. X-ray photoelectron spectroscopy (XPS) experiments were carried out by AXIS ULTRA DLD instrument and the obtained XPS test data were calibrated using the C 1s peak.

2.5 Electrochemical measurements

The electrochemical measurements were performed using the two-electrode cells (CR2032 coin-type half-cells using Na metal as the counter electrode), which were assembled in an argon-filled glove box. The working electrode contained 80 wt% active materials, 10 wt% polyvinylidene fluoride as a binder, and 10 wt% Super P as a conductive additive, which were compressed onto the current collector (copper foil). The electrolyte mainly consisted of 1 M $NaClO_4$ dispersing in dimethyl carbonate/ethylene carbonate (1 : 1 in volume) and 5 vol% of fluoroethylene carbonate was added into the electrolyte solution. The active material loading in the electrode was 0.6–0.8 mg cm^{-2}. The galvanostatic charge–discharge cycle test of the button battery at 3–0.01 V (*vs.* Na^+/Na) was carried out using a LAND test system. For studying the electrochemical behavior of the batteries, cyclic voltammetry (CV) and electrochemical impedance spectroscopy (EIS) were performed using an electrochemical instrument (Zahner IM6, Germany), and the test parameters were set as follows; a scan rate of 0.1 mV s^{-1} at 1.0 mV to 3.0 V and ranging from 10 MHz to 100 kHz at the polarization of 5.0 mV, respectively.

3. Results and discussion

The synthetic route for MoS_2/NSGs-G composite is illustrated in Scheme 1. Firstly, the nitrogen and sulfur co-doped graphene was produced by the electrochemical exfoliation method. After cleaning and impurity removal, cetrimonium bromide, $Na_2MoO_4 \cdot 2H_2O$, and L-cysteine were added to nitrogen and sulfur co-doped graphene mixture solution. Importantly, cetrimonium bromide could improve the charge state on the graphene surface, which promotes the adsorption of graphene to MoO_4^{2-}, thus contributing to MoO_4^{2-} to generate MoS_2 *in situ* on graphene, eventually obtaining self-supporting network structured MoS_2/heteroatom-doped graphene composite (MoS_2/NSGs-G).

The XRD patterns of the as-prepared MoS_2/NSGs-G, MoS_2/Gs-G, bulk MoS_2, and bulk N, S-co-doped graphene are displayed in Fig. 1A. It shows that all diffraction peaks of MoS_2/NSGs-G and MoS_2/Gs-G at about $2\theta = 18.1°$, 32.6°, 39.6°, 58.2°, and 68.8° are well-matched with the (002), (100), (103), (105), and (110) planes of the hexagonal MoS_2 (JCPDS 37-1492).[37] As for bulk MoS_2, all the diffraction peaks were also indexed to the crystal structure of MoS_2 (JCPDS no. 37-1492), and the obvious (002) peak at about $2\theta = 14.1°$ indicated that there was a good layered stacking structure. Compared to bulk MoS_2, although the (002) plane of MoS_2/NSGs-G and MoS_2/Gs-G was located at about $2\theta = 18.1°$, it showed a small right shift to a high scattering angle, demonstrating that MoS_2/NSGs-G and MoS_2/Gs-G still maintained a well-stacked layered structure. The MoS_2/NSGs-G and MoS_2/Gs-G showed a small right shift for the (002) reflection, which is triggered by the intercalation of carbon sheets (amorphous carbon), and graphene between the MoS_2 sheets.[38,39] The bulk N, S-co-doped graphene displays a (002) plane at around 24.2°, which is related to a typical graphite diffraction peak. This peak is slightly left shifted to a low scattering angle, suggesting the presence of a certain oxidation reaction during the electrochemical exfoliation process. A broad peak appearing at around 15.6° corresponded to the characteristic peak of graphene oxide, further confirming that certain oxidation of graphene occurs during electrochemical exfoliation. Apart from this, the typical diffraction peak of graphene at 26.6° in MoS_2/NSGs-G and MoS_2/Gs-G was not detected, indicating that graphene is separated and has not been re-stacked.

The morphology of the MoS_2/NSGs-G sample was characterized by FESEM and TEM techniques. Fig. 1B shows a representative image of the MoS_2/NSGs-G sample, which is composed of intertwined nanosheets with wavy folds on the surface. When the sample is viewed closely in Fig. 1C, it shows that the thickness of the nanosheets is approximately 100 nm. In addition, compared to bulk MoS_2 and bulk N, S-co-doped graphene (shown in Fig. S2B and C†), no large graphene nanosheets and obvious accumulation of MoS_2 were observed in the MoS_2/NSGs-G and MoS_2/Gs-G (seeing in Fig. S2A†)

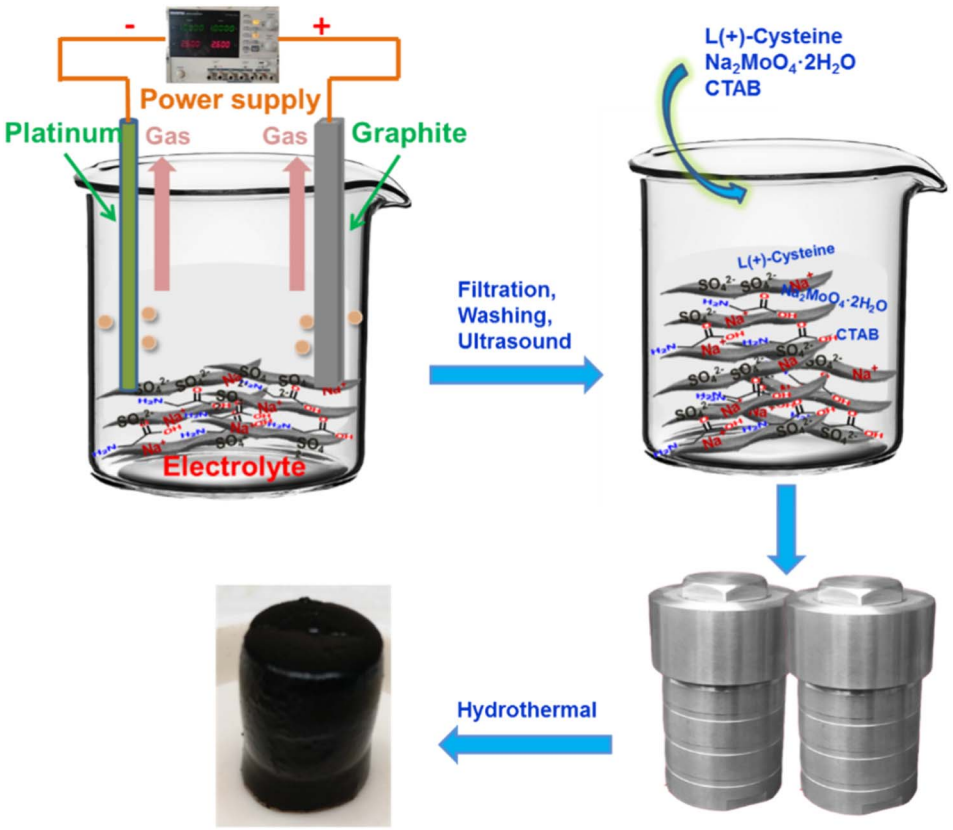

Scheme 1 Schematic illustration of the synthetic route of MoS_2/NSGs-G composite.

samples, suggesting that N, S co-doped graphene acted as a good buffer matrix for MoS_2. Two-dimensional N, S-co-doped graphene, and self-supporting MoS_2 formed a three-dimensional interweaved network structure, which could prevent the re-stacking of N, S-co-doped graphene, and MoS_2 as well as stabilize the structure during cycles. To further

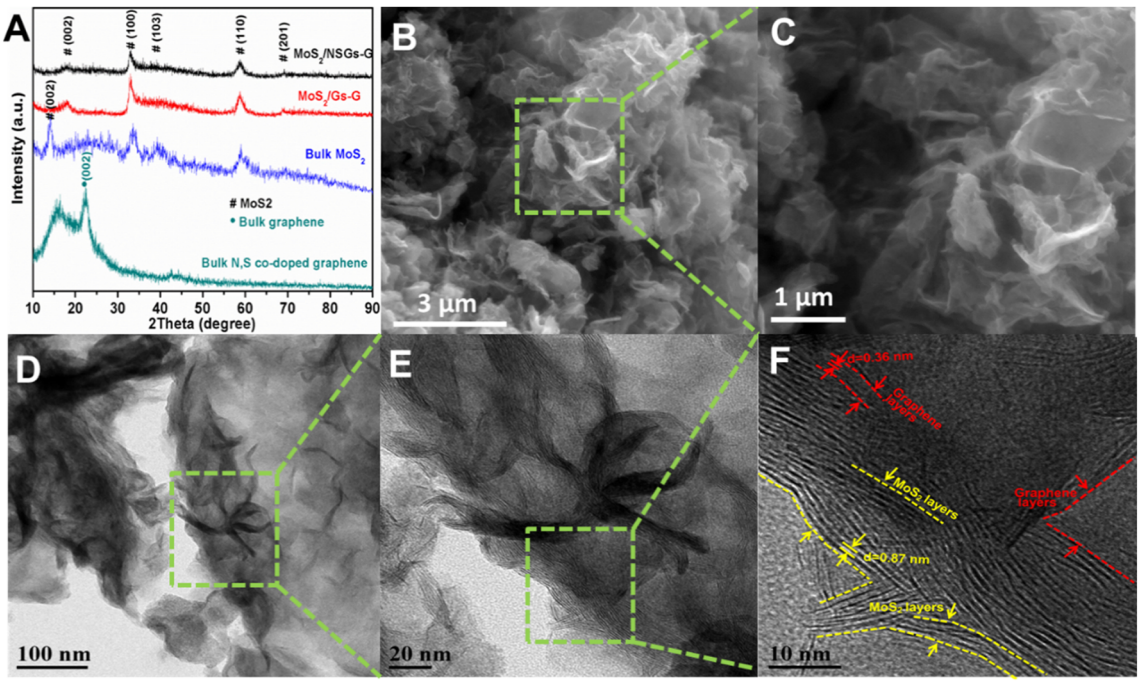

Fig. 1 XRD patterns of MoS_2/NSGs-G, MoS_2/Gs-G, bulk MoS_2 and bulk N, S-co-doped graphene (A), typical SEM (B and C), TEM and HRTEM images (D–F) of MoS_2/NSGs-G sample.

investigate the refined microstructure of MoS_2/NSGs-G, TEM, and HRTEM characterizations were performed. In Fig. 1D and E, it can be seen that there are interweaved ultrathin nanosheets in MoS_2/NSGs-G, and nanosheets are very tightly connected to each other, which is in agreement with the results of SEM. The HRTEM image in Fig. 1F distinctly displays that the MoS_2/NSGs-G sample is consisting of a few layered MoS_2 and graphene and they are interconnected together. The interlayer distances of MoS_2 and graphene are about 0.87 nm and 0.36 nm, respectively. In addition, the detailed element distribution is examined by EDS (demonstrated in Fig. S3†), confirming a uniform distribution of C, O, N, S, and Mo in MoS_2/NSGs-G. It is generally believed that the expanded layer spacing helps accelerate the conduction of electrolytes and ions, increasing the surface area of the material as well as offering abundant reaction sites.[31,33] Therefore, MoS_2/NSGs-G with a self-supporting network structure and expanded layer spacing as the anode has the potential to enhance the sodium ions storage.

The chemical bonding state of the MoS_2/NSGs-G sample was investigated with the XPS technique. Fig. 2A gives strong evidence that there are S, Mo, C, N, and C elements in MoS_2/NSGs-G and their atomic percentage are 22.03%, 8.98%, 54.08%, 3.72%, and 11.18%, respectively. The ratio of S to Mo calculated is about 7.34 to 1, which is higher than the theoretical value of 2 to 1, indicating that sulfur elements have been successfully doped into graphene, which is consistent with the results in Fig. S1.† It can be clearly observed in the XPS results that part of the Mo element is oxidized. Some of the S element is oxidized and some of it is bonded to C. Therefore, according to the results of XPS, we have calculated that the percentage content of MoS_2 in the composite is about 15%. As shown in Fig. 2B, four peaks appeared at about 533.4 eV, 532.4 eV, 531.6 eV, and 530.6 eV in O 1s, which are identified as combining energy peaks of O–C═O, O–C, O═C, and O–H,[40–42] respectively. In the case of C 1s, four peaks at the binding energies of about 289.1 eV, 286.1 eV, 285.0 eV, and 284.4 eV in Fig. 2C, corresponding to the bonding of O–C═O, C–S/C–O, C–N, and sp^2 C, respectively.[43,44] The presence of C–N and C–S further confirmed that nitrogen and sulfur have been doped into the graphene layer. The spectrum of N 1s in Fig. 2D can be divided into four main peaks of about 401.8 eV, 399.7 eV, 398.2 eV, and 395.6 eV, which are related to graphitic N, pyrrole N, pyridine N, and Mo 3p, respectively.[41,45] The result of the N 1s peak provides strong evidence that nitrogen has been successfully doped into graphene and it could improve the electronic conductivity of the composite effectively. Furthermore, pyridinic N and pyrrolic N could offer extra active sites and defects, which contributes to enhancing Na^+ storage capacity.[46] As for the S 2P spectrum in Fig. 2E, it shows that the peaks at 163.7 eV and 162.5 eV correspond to S $2p_{1/2}$ and S $2p_{3/2}$, respectively,[47] and the sulfur oxide peak is observed at 169.1 eV, indicating that sulfur partially exists in the form of S^{2+} in MoS_2/NSGs-G.[48] The spectrum of Mo 3d in Fig. 2F shows that the peaks at 232.9 eV, 229.7 eV, and 227.0 eV correspond to Mo $3d_{3/2}$, Mo $3d_{5/2}$, and S 2s, respectively,[49] which are related to S^{2-} and Mo^{4+} ions in MoS_2.[50] In addition, the peak at about 236.3 eV belongs to Mo^{6+}, which is due to the partial oxidation of the surface of MoS_2/NSGs-G in air.[51] Besides, the total atomic percentages of N and S were detected as 1.38% and 14.95% in MoS_2/NSGs-G, respectively. It is believed that N or S doping could regulate the charge state of the material and increase the active sites, which are conducive to enhancing the Na^+ diffusion rate and charge transport in the materials.

To investigate the electrochemical behavior of MoS_2/NSGs-G electrode, the typical charge–discharge tests at 0.5 A g^{-1} were performed by the LAND test system (it needs to be pointed out that the cells are activated using 0.025 A g^{-1}, 0.05 A g^{-1}, and 0.1 A g^{-1} in the first, second, and third charge–discharge

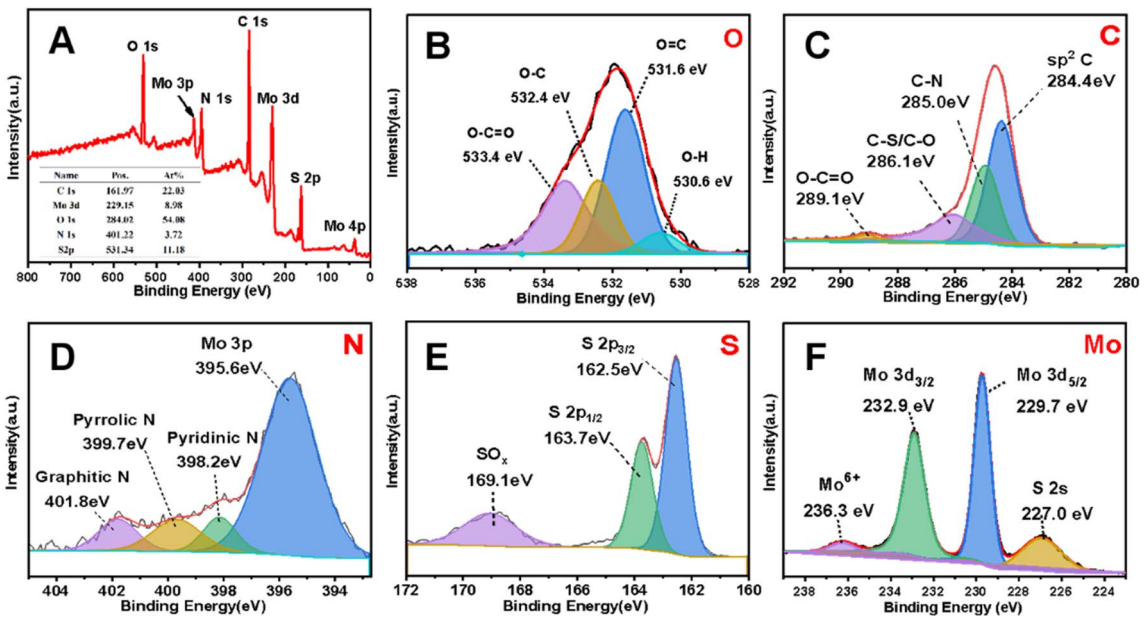

Fig. 2 XPS spectra of the MoS_2/NSGs-G (A) and the corresponding high-resolution of O 1s (B), C 1s (C), N 1s (D), S 2p (E), and Mo 3d (F).

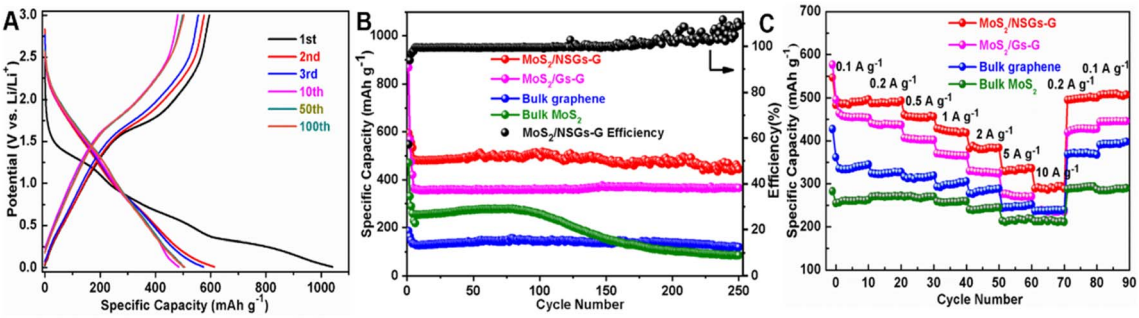

Fig. 3 Representative charge–discharge curves of MoS_2/NSGs-G electrode at 0.1 A g^{-1} (A), cycling performances at the current density of 0.5 A g^{-1} (B) and rate capability at different current density (C) of the MoS_2/NSGs-G, MoS_2/Gs-G, bulk N, S-co-doped graphene and bulk MoS_2 electrodes.

process, respectively. The discharge process represents the sodiation process). For the first sodiation process, there are three inclined voltage platforms in the range of 1.28–1.19 V, 0.92–0.37 V, and 0.29–0.03 V, as shown in Fig. 3A, which are attributed to the formation of the SEI layer, the reaction of sodium ions into the MoS_2 layers and the sodium ions embedded graphene layers, respectively. The voltage platform appears near 1.65–2.21 V in the initial anodic process, which is mainly the process of sodium ion extraction from Na_xMoS_2. In the subsequent charge–discharge processes, the MoS_2/NSGs-G electrode presents two stable voltage platforms at around 1.60–0.85 V and 1.78–2.23 V, which belong to the sodiation reactions of Na insertion into S and the reactions of Na_2S conversion into S, respectively. In addition, the MoS_2/NSGs-G electrode displays discharge and charge capacities of 1040.4 and 595.7 mA h g^{-1} during the initial cycle, respectively, and the initial coulombic efficiency was 52.4%. The lost capacity may be due to the formation of solid electrolyte interphase (SEI) or the decomposition of electrolyte.[52] As the cycles continue, the coulombic efficiency of MoS_2/GNs-AG in the second and third cycles rapidly reached 94.0% and 96.7%, which indicates that the electrode has high cycle reversibility. In particular, the MoS_2/NSGs-G electrode maintains relatively high sodium storage with a charge capacity of about 502.8 mA h g^{-1} after 100 cycles. Compared with the specific capacity of the first charge, the capacity retention rate after 100 cycles was still maintained at 84.4%, implying that the insertion/extraction process of sodium in the MoS_2/NSGs-G electrode is highly reversible.

Fig. 3B presents the continuous galvanostatic charge–discharge cycling performance of the MoS_2/NSGs-G, MoS_2/Gs-G, bulk N, S-co-doped graphene, and bulk MoS_2 electrodes. As can be noticed, the bulk MoS_2 electrode shows poor cycle performance and the cycle begins to decay rapidly after about 100 cycles. Even the specific capacity of sodium storage decreased rapidly from 256.7 mA h g^{-1} to 85.9 mA h g^{-1} after 250 cycles. This result may be caused by large volume expansion of MoS_2, leading to the pulverization and exfoliation of MoS_2, ultimately resulting in reducing the specific capacity of the electrode and cycle performance degradation. Distinctly, the other three electrodes display extremely stable electrochemical performances for sodium storage, which indicates that graphene has an important role in the cycle stability of the electrode. The charge-specific capacity of MoS_2/Gs-G and bulk N, S-co-doped graphene electrodes after 250 cycles are 365.7 mA h g^{-1} and 120.0 mA h g^{-1}, respectively, which are higher than the charge capacity of the bulk MoS_2 electrode. Among them, the MoS_2/NSGs-G electrode delivers the highest sodium storage capacity with a specific capacity of 443.9 mA h g^{-1} after 250 cycles at the current density of 0.5 A g^{-1}. The capacity of MoS_2/NSGs-G fluctuates slightly, which may be due to the existence of unevenly growing solid electrolyte interphase (SEI) during the cycles, leading to a partial irreversible reaction. In addition, because of the volume effect of MoS_2, a small part of the active material loosens or falls off during the sodiation/desodiation process, which may also cause fluctuations in the capacity of the composite material. Even though the capacity of the MoS_2/NSGs-G fluctuates slightly, the coulombic efficiency of MoS_2/NSGs-G except in the first three cycles is about 99%, indicating that MoS_2/NSGs-G has excellent reversibility. The MoS_2/NSGs-G electrode has a satisfactory reversible sodium storage capacity and extremely stable cycling performance, which are attributed to the nitrogen and sulfur co-doping increasing the sodium storage sites and a three-dimensional interconnected network that can stabilize the structure of the electrode material. Meanwhile, the synergistic effect of N, S-co-doped graphene and high theoretical specific capacity MoS_2 makes the MoS_2/NSGs-G composite material possess an extremely high specific capacity and superior cycling performance.

Fig. 3C displays the impressive rate performances of MoS_2/NSGs-G, MoS_2/Gs-G, bulk N, S-co-doped graphene, and bulk MoS_2 electrodes at different current densities from 0.1 to 10 A g^{-1}, and finally changed back to 0.1 A g^{-1}. It is distinctly seen that all electrodes reveal relatively stable capacity at each current density. However, the rate performance of bulk MoS_2 electrodes is worse than that of other electrodes, and its specific capacity is lower than that of other electrodes at each rate. This may be put down to the lack of N, S co-doped graphene as a buffer to support molybdenum disulfide, which is difficult to withstand the "shock" caused by current changes, ultimately leading to the decrease of specific capacity. In Fig. 3C, as the current density returns to its initial value, the corresponding capacity increases may be attributed to the high reversibility

and the activation process of bulk MoS_2 and graphene.[53] Clearly, the MoS_2/NSGs-G electrode demonstrated the best rate performance, with a reversible charge capacity of 491.5, 490.5, 453.9, 418.1, 383.8, 333.1, and 294.4 mA h g^{-1} at 0.1, 0.2, 0.5, 1, 2, 5, and 10 A g^{-1}, respectively (provided in the Table S1†). When the current density recovered to 0.1 A g^{-1} again, the MoS_2/NSGs-G electrode still maintained the specific capacity of 507.3 mA h g^{-1}, which fully demonstrates that the MoS_2/NSGs-G sample has good structural stability and excellent rate performance. These results indicate that the MoS_2/NSGs-G sample has potential research significance and application prospects in high-performance SIBs.

In order to understand the electrochemical behavior of sodium-ion storage for MoS_2/NSGs-G electrode, the CV test was implemented and the results are presented in Fig. 4A. It reveals that three reduction peaks appearing at about 0.01 V, 0.46 V (disappearing in the subsequent cycles), and 1.07 V are assigned to Na^+ insertion into the graphene layers,[54] the formation of SEI layers (decomposition of electrolyte) and the insertion of sodium ions into MoS_2 in the initial cathodic scan,[33,55] respectively. In the first anodic process, there are two oxidation peaks at approximately 1.76 V and 2.23 V, which are related to the reconstitution of S and Mo to form MoS_2 and the Na^+ de-insertion from Na_2S,[26,37] respectively. In the two subsequent cycles, the CV curve demonstrates that the oxidation peak and the reduction peak are highly coincident without significant changes, suggesting that MoS_2/NSGs-G electrode possesses very stable and high reversibility of electrochemical behavior.

To further inquire the electrochemical reaction kinetics of the MoS_2/NSGs-G electrode, CV curves at various scanning rates from 0.1 mV to 1.0 mV s^{-1} were obtained, as shown in Fig. 4B. Although there is a certain polarization of the redox peak of the MoS_2/NSGs-G electrode with the increase of scanning rate, significant reduction peak, and oxidation peak at around 0.65 V and 1.81 V, relating to the reversible process of sodiation and desodiation, respectively, are still observed, which is highly consistent with the analysis results shown in Fig. 4A. According to previous research results, it is believed that there is a power-law relationship between current and sweep speed, which obeys the following equation:[55,56]

$$i = av^b \quad (1)$$

where a and b stand for adjustable parameters, v is on behalf of the scan speed, i represents the current density. Particularly, when the value of b is close to 0.5 or 1, signifying the diffusion-controlled process or the capacitive behavior is dominant in the electrode.[57,58] Fig. 4C presents the values of b at peak 1 and peak 2 as 0.87 and 0.90, respectively, indicating a capacitive storage mechanism is more dominant in the MoS_2/NSGs-G electrode, making for a fast Na^+ sodiation/desodiation and prominent rate performance. These results are highly consistent with the

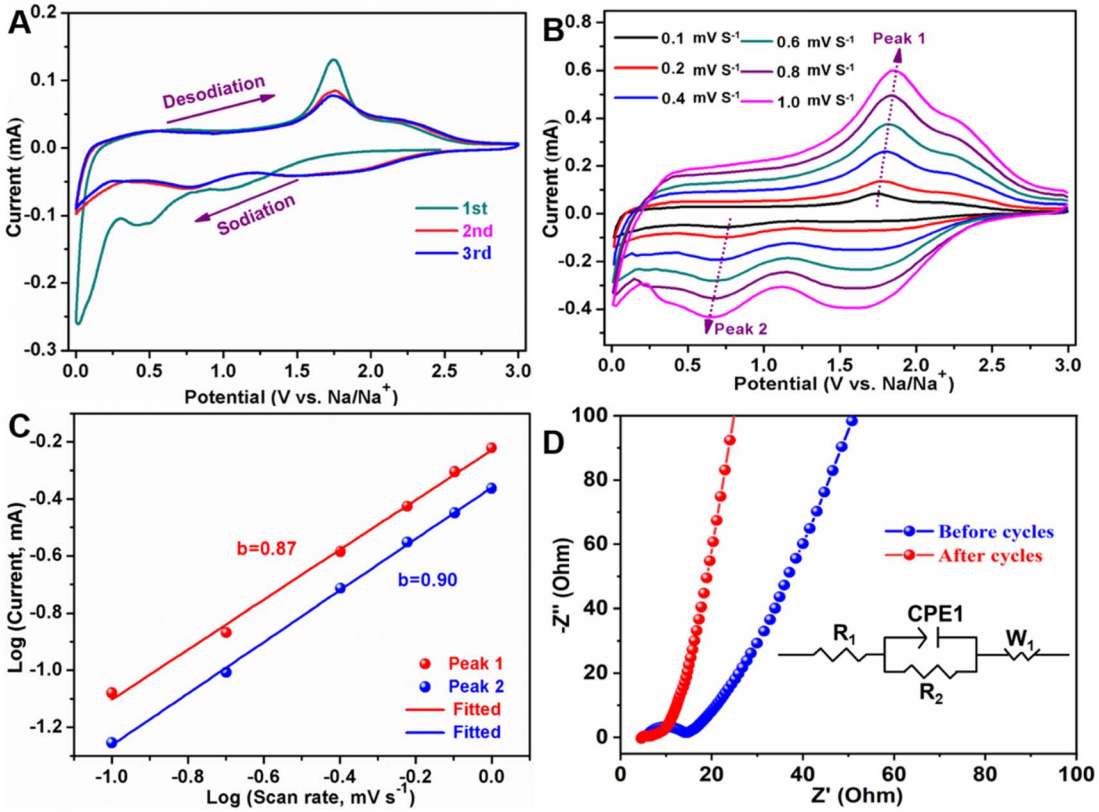

Fig. 4 Typical CV curves at a sweep rate of 0.1 mV s^{-1} for the first three cycles (A), CV curves at different scan rates (B), log(*i*) *versus* log(*v*) plots at around 0.6 V (sodiation) and at around 1.8 V (desodiation) of MoS_2/NSGs-G (C), Nyquist plots for electrochemical impedance spectra of MoS_2/NSGs-G before and after cycles, the inset is the equivalent circuit of Nyquist plots (D).

analysis in Fig. 3C, providing strong evidence that the MoS_2/NSGs-G material has outstanding rate performance. The EIS results in Fig. 4D exhibit that the MoS_2/NSGs-G electrode displays a semicircle in the high-frequency area and a sloping straight line in the low-frequency area before and after 3 cycles, which are related to charge transfer resistance (R_{ct}) and Warburg resistance (Z_w). It can be obviously seen that the charge transfer resistance of the MoS_2/NSGs-G electrode after 3 cycles (9 Ω) is smaller than that of the electrode before cycles (15 Ω). This may be because the composite material forms a stable SEI during the cycles, layered nanostructure heteroatom doped graphene could effectively alleviate the volume effect of MoS_2 and stabilize the structure of composite materials, which are conducive to reducing the resistance of the composite material. According to equation[59] $i_0 = RT/nFR_{ct}$, the exchange current density is used to assess the electrochemical performance of the electrode. Where T refers to the absolute temperature, n stands for the number of transferred electrons, R (8.314 J mol^{-1} K^{-1}) represents the gas constant, and F (96 485 C mol^{-1}) and R_{ct} are referred to as the Faraday constant and charge transfer resistance, respectively. The values of i_0 for the MoS_2/NSGs-G electrode before and after 3 cycles are 1.71×10^{-5} A cm^{-2} and 2.85×10^{-3} A cm^{-2}, respectively. Therefore, the above results show that the MoS_2/NSGs-G has good reaction reversibility and low resistance.

In order to investigate the capacitive effects (k_1v) and the diffusion-controlled insertion process ($k_2v^{1/2}$) of MoS_2/NSGs-G, a function of potential is used following:[60,61]

$$i(V) = k_1v + k_2v^{1/2} \quad (2)$$

where v stands for the scan rate. It is usually used to distinguish the ratio of the current related to surface capacitance and sodium ion semi infinite linear diffusion by determining the value of k_1 and k_2. Fig. 5A exhibits that 81% (orange) of the total capacity represents the capacitive contribution for the MoS_2/NSGs-G sample at a scan rate of 0.1 mV s^{-1}, which is well coincident with the value of b. As a comparison, the results of the capacitive contribution of MoS_2/NSGs-G electrode at different scan rates of 0.2, 0.4, 0.6, 0.8, and 1 mV s^{-1} are provided in Fig. S4,† further indicating that the MoS_2/NSGs-G electrode has an outstanding characteristic of capacitive charge storage contribution. With the increase in the sweep rate, Fig. 5B displays that the diffusion behavior of MoS_2/NSGs-G electrode has decreased, while the capacitive charge storage contribution increased, which are 87%, 91%, 94%, 95%, and 98% of the total capacity contribution. Up to 98% of the pseudocapacitance is mainly attributed to the ultrathin layer nanostructures of MoS_2/NSGs-G effectively restraining the aggregation of MoS_2 and graphene so that Na^+ can be rapidly inserted and extracted from the material surface during the cycles.[62] In addition, the high specific surface area, abundant defects, and heteroatoms of nitrogen and sulfur in the composite material are helpful to improve the electrochemical performance and facilitate the pseudocapacitance behavior. Moreover, the synergistic effects of MoS_2 and graphene contribute to enhancing the interface storage and the sodiation/desodiation reaction, which makes the composite material show an obvious pseudocapacitance behavior.[46] These results strongly demonstrate that MoS_2/NSGs-G possesses the sodium storage mechanism of dominant pseudocapacitive contribution, which plays a critical role in improving the electrochemical properties of electrode materials.[63,64]

In order to investigate the crystal structure and morphological changes of the MoS_2/NSGs-G electrode after cycles, XRD, SEM, and HRTEM studies on the MoS_2/NSGs-G electrode after the cycles were performed. Fig. 6A shows the XRD pattern of MoS_2/NSGs-G after 250 cycles. It can be clearly observed that the diffraction peaks of the MoS_2/NSGs-G at about $2\theta = 43.2°$, 50.3°, and 70.0° are well referred to the (111), (200), and (220) planes of the copper substrate. Two obvious diffraction peaks appeared at around 21.1° and 28.4°, which point to the products of $NaMoS_2$ and Na_2S, respectively. In addition, three diffraction peaks in the (002), (100), and (103) planes were observed, which well matched those of the standard MoS_2 (PDF # 37-1492), indicating that MoS_2 can still maintain good crystal structure even after the cycles.[65,66] Fig. 6B and C show the morphologies of the MoS_2/NSGs-G electrode before and after cycles, respectively.

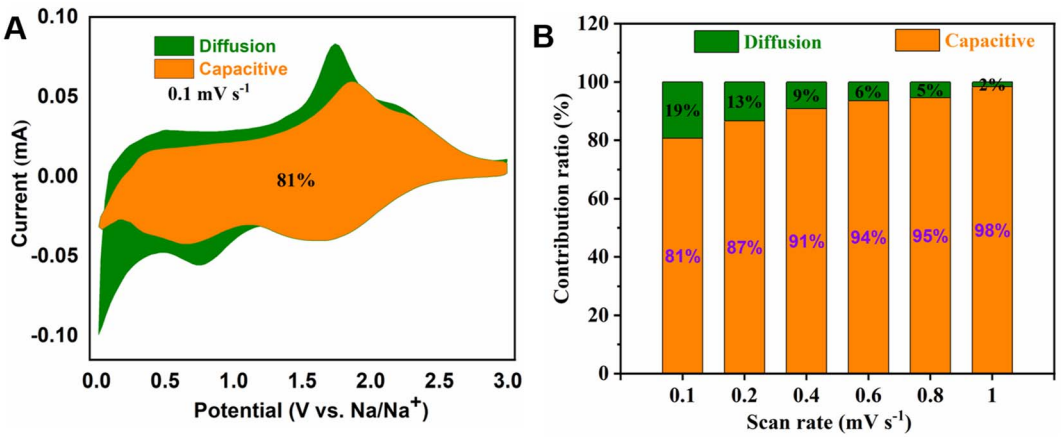

Fig. 5 Capacitive charge storage contribution (orange) and diffusion charge storage contribution (olive) at 0.1 mV s^{-1} (A), normalized contribution ratio of capacitive (orange) and diffusion-controlled (olive) capacities at different sweep rates (B).

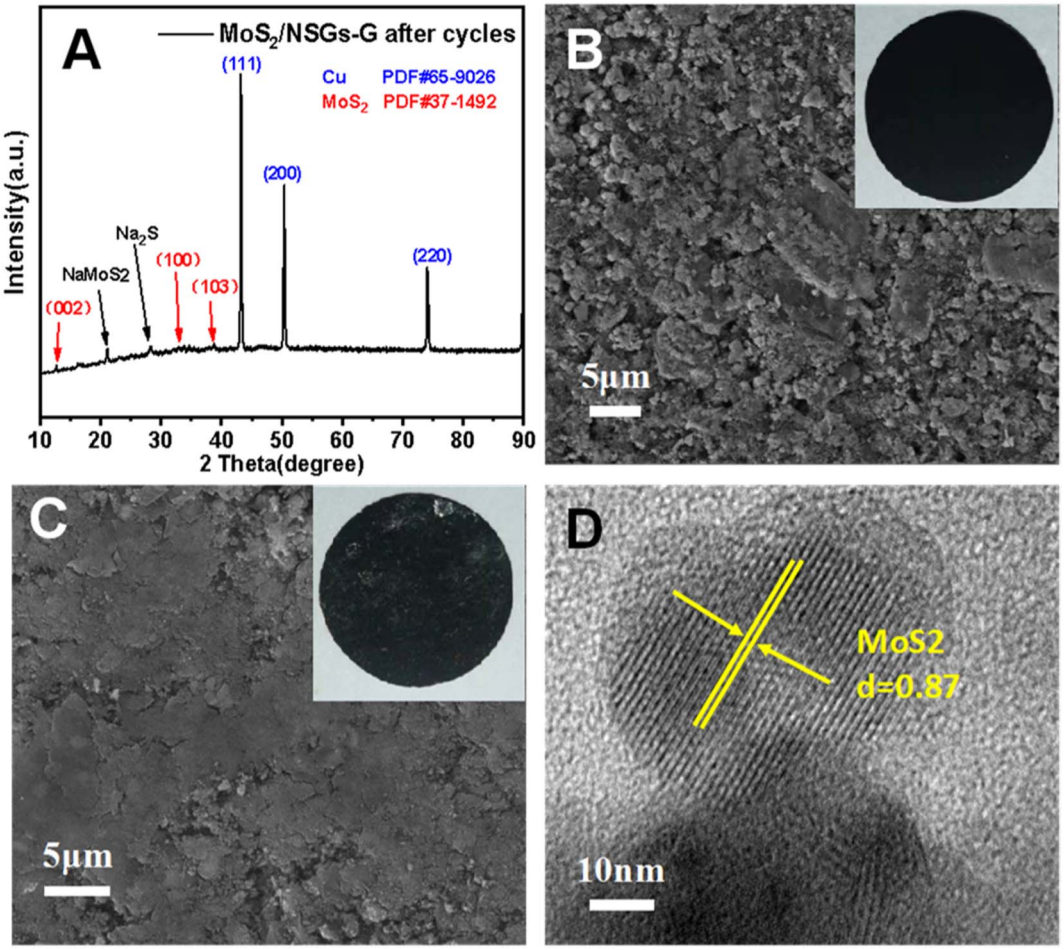

Fig. 6 XRD pattern of the MoS_2/NSGs-G after 250 cycles (A), SEM images of the MoS_2/NSGs-G electrode before 250 cycles (B), after 250 cycles (C), HRTEM image of the MoS_2/NSGs-G after 250 cycles (D). Inset: corresponding digital photo of the MoS_2/NSGs-G electrode before and after 250 cycles in SIBs.

The original MoS_2/NSGs-G electrode before cycles has a rough surface and there are many gaps between particles. After cycles, the surface of the MoS_2/NSGs-G electrode becomes smooth and the particles are tightly connected with each other. No cracks appeared on the surface of the MoS_2/NSGs-G electrode, indicating that the composite still maintained good structural stability after long cycles. Moreover, the solid electrolyte film generated on the electrode surface is also helpful to protect the structure of the material. In Fig. 6D, the HRTEM image of the MoS_2/NSGs-G electrode shows that the lattice fringe of MoS_2 can be obviously observed, which still remained at 0.87 nm after cycles, indicating that the MoS_2/NSGs-G possesses good structural stability. Therefore, because of the good structural stability of the MoS_2/NSGs-G, it could contribute to improving the cyclic stability and the electrochemical performance of the material.

The MoS_2/NSGs-G material has remarkable electrochemical properties of high sodium storage capacity, excellent rate performance and long cycle life are on account of several obvious structural characteristics (i) two-dimensional structure of graphene and MoS_2 spontaneously assemble into a self-supporting three-dimensional network structured composite material, this three-dimensional network could alleviate the volume change of the material, stabilize the structure during cycles and shorten the transport path of the ions and electrolyte, (ii) heteroatomic N and S are uniformly doped on graphene nanosheets by a facile electrochemical exfoliation, increasing the reaction sites, electronic conductivity and sodium storage capacity, (iii) extended layer spacing of graphene and MoS_2, which facilitates increased sodium storage capacity, ions and electrolyte transport, (iv) the high sodium storage capacity of MoS_2 and good support matrix of graphene are closely intertwined and create a synergistic effect, making the composite have outstanding electrochemical properties. As a result, this work may offer an operable strategy to explore high-performance MoS_2-based composites for SIBs and other potential applications in the catalytic field.

4. Conclusions

In summary, we presented a scalable strategy to prepare a self-supporting network structured MoS_2/heteroatom-doped graphene as an anode for SIBs, through a facile electrochemical

exfoliation-hydrothermal route. This strategy allowed nitrogen and sulfur to be successfully and uniformly doped in graphene. Meanwhile, few-layered graphene and MoS_2 are intertwined to form a self-supporting three-dimensional network structure. When investigating the electrochemical performances as an anode for SIBs, the MoS_2/NSGs-G electrode exhibits satisfactory electrochemical stability with a reversible capacity of 443.9 mA h g^{-1} after 250 cycles at 0.5 A g^{-1}. The MoS_2/NSGs-G composite also demonstrates a desirable rate performance, with the charge capacity of 491.5, 490.5, 453.9, 418.1, 383.8, 333.1, and 294.4 mA h g^{-1} at 0.1, 0.2, 0.5, 1, 2, 5 and 10 A g^{-1}, respectively. Moreover, the MoS_2/NSGs-G composite revealed a dominant pseudocapacitive contribution and faster sodium ion interface kinetics characteristic. Therefore, the MoS_2/NSGs-G would be one of the potential anode materials for enhancing the electrochemical performance of SIBs.

Conflicts of interest

There are no conflicts to declare.

Acknowledgements

This study is supported by the Guangxi Natural Science Foundation (2020GXNSFAA297019 and 2019GXNSFBA245099), Doctoral Fund of Guangxi University of Science and Technology (19Z11), Guangxi Key Laboratory of Low Carbon Energy Material (2020GKLLCEM01), Guangxi Key Laboratory of Automobile Components and Vehicle Technology (2022GKLACVTZZ05) and Innovation Training Program for College Students (202210594006).

References

1 J. Li, W. Gao, L. Huang, Y. Jiang, X. Chang, S. Sun and L. Pan, *Appl. Surf. Sci.*, 2022, **571**, 151307.
2 M. Liu, N. Li, S. Wang, Y. Li, C. Liang and K. Yu, *J. Alloys Compd.*, 2023, **933**, 167689.
3 M. Cao, Y. Feng, P. Zhang, L. Yang, X. Gu and J. Yao, *J. Alloys Compd.*, 2022, **907**, 164499.
4 Y. Jin, S. Tan, Z. Zhu, Y. He, L. Quoc Bao, P. Saha and Q. Cheng, *Appl. Surf. Sci.*, 2022, **598**, 153778.
5 L. Hu, X. Hu, Z. Lin and Z. Wen, *ChemElectroChem*, 2018, **5**, 1552–1558.
6 Y. Li, J. Song, R. Tong, X. Lu, Q. Tian, J. Chen and L. Yang, *J. Alloys Compd.*, 2022, **901**, 163563.
7 J. Lin, Y.-H. Shi, Y.-F. Li, X.-L. Wu, J.-P. Zhang, H.-M. Xie and H.-Z. Sun, *Chem. Eng. J.*, 2022, **428**, 131103.
8 X. Hao, J. Zhang, J. Wang, B. Zhao, M. Qian, R. Wang, Q. Yuan, X. Zhang, X. Huang, H. Li, C. Yu, J. Xie, F. Wu and G. Tan, *Nano Energy*, 2022, **103**, 107850.
9 X. Cheng, Q. Bai, H. Li, H. Dou, Z. Zhao, D. Bian and X. Wang, *Chem. Eng. J.*, 2022, **442**, 136222.
10 L. Fan, X. Li, X. Song, N. Hu, D. Xiong, A. Koo and X. Sun, *ACS Appl. Mater. Interfaces*, 2018, **10**, 2637–2648.
11 H. Chen, T. Song, L. Tang, X. Pu, Z. Li, Q. Xu, H. Liu, Y. Wang and Y. Xia, *J. Power Sources*, 2020, **445**, 227271.
12 H. Dai, M. Tang, J. Huang and Z. Wang, *ACS Appl. Mater. Interfaces*, 2021, **13**, 10870–10877.
13 M. Feng, H. Zhang, Y. Zhang, M. Zhang and H. Feng, *ChemistrySelect*, 2019, **4**, 6148–6154.
14 B. Sun, Q. Lu, K. Chen, W. Zheng, Z. Liao, N. Lopatik, D. Li, M. Hantusch, S. Zhou, H. I. Wang, Z. Sofer, E. Brunner, E. Zschech, M. Bonn, R. Dronskowski, D. Mikhailova, Q. Liu, D. Zhang, M. Yu and X. Feng, *Adv. Mater.*, 2022, **34**, 2108682.
15 Z. Tang, S. Zhou, P. Wu, H. Wang, Y. Huang, Y. Zhang, D. Sun, Y. Tang and H. Wang, *Chem. Eng. J.*, 2022, **441**, 135899.
16 L. Yan, J. Wang, Q. Ren, L. Fan, B. Liu, L. Zhang, L. He, X. Mei and Z. Shi, *Chem. Eng. J.*, 2022, **432**, 133257.
17 H. Zhang, W. Zhang and F. Huang, *Chem. Eng. J.*, 2022, **434**, 134503.
18 Y. Zhao, Z. Hu, C. Fan, Z. Liu, R. Zhang, S. Han, J. Liu and J. Liu, *Chem. Eng. J.*, 2022, **446**, 137427.
19 Q. Lu, A. Omar, L. Ding, S. Oswald, M. Hantusch, L. Giebeler, K. Nielsch and D. Mikhailova, *J. Mater. Chem. A*, 2021, **9**, 9038–9047.
20 H. Lim, S. Yu, W. Choi and S. O. Kim, *ACS Nano*, 2021, **15**, 7409–7420.
21 Y. Liu, Y. Yang, X. Wang, Y. Dong, Y. Tang, Z. Yu, Z. Zhao and J. Qiu, *ACS Appl. Mater. Interfaces*, 2017, **9**, 15484–15491.
22 Y. Wang, Y. Wang, Y. X. Wang, X. Feng, W. Chen, J. Qian, X. Ai, H. Yang and Y. Cao, *ACS Appl. Mater. Interfaces*, 2019, **11**, 19218–19226.
23 M. Shao, Y. Cheng, T. Zhang, S. Li, W. Zhang, B. Zheng, J. Wu, W. W. Xiong, F. Huo and J. Lu, *ACS Appl. Mater. Interfaces*, 2018, **10**, 33097–33104.
24 Y. Rao, J. Wang, P. Liang, H. Zheng, M. Wu, J. Chen, F. Shi, K. Yan, J. Liu, K. Bian, C. Zhang and K. Zhu, *Chem. Eng. J.*, 2022, **443**, 136080.
25 H. Qiu, H. Zheng, Y. Jin, M. Jia, Q. Yuan, C. Zhao and M. Jia, *Ionics*, 2020, **26**, 5543–5551.
26 Z. Xiao, W. Chen, Z. chen, C. Chen, W. Cao and F. Yu, *Energy Fuels*, 2022, **36**, 3954–3963.
27 Y. Teng, H. Zhao, Z. Zhang, Z. Li, Q. Xia, Y. Zhang, L. Zhao, X. Du, Z. Du, P. Lv and K. Swierczek, *ACS Nano*, 2016, **10**, 8526–8535.
28 J. Wu, J. Liu, J. Cui, S. Yao, M. Ihsan-Ul-Haq, N. Mubarak, E. Quattrocchi, F. Ciucci and J.-K. Kim, *J. Mater. Chem. A*, 2020, **8**, 2114–2122.
29 B. Ye, L. Xu, W. Wu, Y. Ye, Z. Yang, Y. Qiu, Z. Gong, Y. Zhou, Q. Huang, Z. Shen, Z. Hong, Z. Meng, Z. Zeng, Z. Cheng, S. Ye, H. Hong, Q. Lan, F. Li, T. Guo and S. Xu, *ACS Sustainable Chem. Eng.*, 2022, **10**, 3166–3179.
30 X. Zhang, K. Liu, S. Zhang, F. Miao, W. Xiao, Y. Shen, P. Zhang, Z. Wang and G. Shao, *J. Power Sources*, 2020, **458**, 228040.
31 F. He, C. Tang, Y. Liu, H. Li, A. Du and H. Zhang, *J. Mater. Sci. Technol.*, 2022, **100**, 101–109.
32 G. Sahoo, S. R. Polaki, S. Ghosh, N. G. Krishna, M. Kamruddin and K. Ostrikov, *Energy Storage Mater.*, 2018, **14**, 297–305.

33 S. Liang, S. Zhang, Z. Liu, J. Feng, Z. Jiang, M. Shi, L. Chen, T. Wei and Z. Fan, *Adv. Energy Mater.*, 2021, **11**, 2002600.
34 G. Li, D. Luo, X. Wang, M. H. Seo, S. Hemmati, A. Yu and Z. Chen, *Adv. Funct. Mater.*, 2017, **27**, 1702562.
35 S. R. Polaki, G. Sahoo, P. Anees, N. G. Krishna, M. Kamruddin and S. Dhara, *Appl. Surf. Sci.*, 2021, **545**, 149045.
36 S. Sahoo, G. Sahoo, S. M. Jeong and C. S. Rout, *J. Energy Storage*, 2022, **53**, 1052122.
37 X. Zhao, G. Wang, X. Liu, X. Zheng and H. Wang, *Nano Res.*, 2018, **11**, 3603–3618.
38 G. Yang, X. Li, Y. Wang, Q. Li, Z. Yan, L. Cui, S. Sun, Y. Qu and H. Wang, *Electrochim. Acta*, 2019, **293**, 47–59.
39 J. Wang, C. Luo, T. Gao, A. Langrock, A. C. Mignerey and C. Wang, *Small*, 2015, **11**, 473–481.
40 Y. C. G. Kwan, G. M. Ng and C. H. A. Huan, *Thin Solid Films*, 2015, **590**, 40–48.
41 X. Zhang, Y. Wang and G. Wen, *J. Solid State Chem.*, 2020, **292**, 121718.
42 Y. Liu, *Int. J. Electrochem. Sci.*, 2018, **13**, 2054–2068.
43 S. Kandula, B. Sik Youn, J. Cho, H.-K. Lim and J. Gon Son, *Chem. Eng. J.*, 2022, **439**, 135678.
44 S. Xu, Q. Zhu, T. Chen, W. Chen, J. Ye and J. Huang, *Mater. Chem. Phys.*, 2018, **219**, 399–410.
45 T. Tang, T. Zhang, L. Zhao, B. Zhang, W. Li, J. Xu, L. Zhang, H. Qiu and Y. Hou, *Mater. Chem. Front.*, 2020, **4**, 1483–1491.
46 X. Dong, Z. Xing, G. Zheng, X. Gao, H. Hong, Z. Ju and Q. Zhuang, *Electrochim. Acta*, 2020, **339**, 135932.
47 W. Wang, S. Guo, P. Zhang, J. Liu, C. Zhou, J.-J. Zhou, L. Xu, F. Chen and L. Chen, *ACS Appl. Energy Mater.*, 2021, **4**, 5775–5786.
48 H. Ji, S. Hu, Z. Jiang, S. Shi, W. Hou and G. Yang, *Electrochim. Acta*, 2019, **299**, 143–151.
49 Q. Pan, Q. Zhang, F. Zheng, Y. Liu, Y. Li, X. Ou, X. Xiong, C. Yang and M. Liu, *ACS Nano*, 2018, **12**, 12578–12586.
50 B. Xie, Y. Chen, M. Yu, T. Sun, L. Lu, T. Xie, Y. Zhang and Y. Wu, *Carbon*, 2016, **99**, 35–42.
51 X. Zhang, T. Ma, T. Fang, Y. Gao, S. Gao, W. Wang and L. Liao, *J. Alloys Compd.*, 2020, **818**, 152821.
52 L. Jing, J. Sun, C. Sun, D. Wu, G. Lian, D. Cui, Q. Wang and H. Yu, *Nano Res.*, 2023, **16**, 473–480.
53 D. Sun, D. Ye, P. Liu, Y. Tang, J. Guo, L. Wang and H. Wang, *Adv. Energy Mater.*, 2017, **8**, 1702383.
54 G. Ma, Z. Xiang, K. Huang, Z. Ju, Q. Zhuang and Y. Cui, *Part. Part. Syst. Charact.*, 2017, **34**, 1600315.
55 S. Li, Y. Li, Z. Zhao, F. Wang, X. Bao, C. Hao, Z. Tang and Y. Yang, *ACS Appl. Nano Mater.*, 2021, **4**, 10257–10266.
56 F. Chen, J. Yuan, M. Zhou, H. Gui, Y. Xiang, J. Yang, X. Li, C. Xu and R. Wang, *ACS Appl. Energy Mater.*, 2022, **5**, 7249–7259.
57 H. Li, X. Qian, C. Xu, S. Huang, C. Zhu, X. Jiang, L. Shao and L. Hou, *ACS Appl. Mater. Interfaces*, 2017, **9**, 28394–28405.
58 D. Chao, P. Liang, Z. Chen, L. Bai, H. Shen, X. Liu, X. Xia, Y. Zhao, S. V. Savilov, J. Lin and Z. X. Shen, *ACS Nano*, 2016, **10**, 10211–10219.
59 P. Guo, H. Song and X. Chen, *Electrochem. Commun.*, 2009, **11**, 1320–1324.
60 P. Li, Y. Yang, S. Gong, F. Lv, W. Wang, Y. Li, M. Luo, Y. Xing, Q. Wang and S. Guo, *Nano Res.*, 2018, **12**, 2218–2223.
61 Y. Luo, X. Ding, X. Ma, D. Liu, H. Fu and X. Xiong, *Electrochim. Acta*, 2021, **388**, 138612.
62 X. Yuan, S. Qiu and X. Zhao, *ACS Appl. Mater. Interfaces*, 2021, **13**, 34238–34247.
63 X. Xiang, Q. Lu, M. Han and J. Chen, *Chem. Commun.*, 2016, **52**, 3653–3656.
64 G. Sahoo, S. Polaki, P. Anees, S. Ghosh, S. Dhara and M. Kamruddin, *Phys. Chem. Chem. Phys.*, 2019, **21**, 25196–25205.
65 Y. X. Wang, S. L. Chou, D. Wexler, H. K. Liu and S. X. Dou, *Chem.–Eur. J.*, 2014, **20**, 9607–9612.
66 L. David, R. Bhandavat and G. Singh, *ACS Nano*, 2014, **8**, 1759–1770.